HHS Public Access

Author manuscript

Sens Actuators B Chem. Author manuscript; available in PMC 2021 July 15.

Published in final edited form as:

Sens Actuators B Chem. 2018 November 10; 273: 1694–1704. doi:10.1016/j.snb.2018.07.044.

Anti-biofouling implantable catheter using thin-film magnetic microactuators

Qi Yang[a,b,c], **Hyunsu Park**[a,b,c], **Tran N.H. Nguyen**[a,b,c], **Jeffrey F. Rhoads**[b,d,e], **Albert Lee**[g], **R. Timothy Bentley**[f], **Jack W. Judy**[h], **Hyowon Lee**[a,b,c,*]

[a]Weldon School of Biomedical Engineering, Purdue University, West Lafayette, IN 47907, USA

[b]Birck Nanotechnology Center, Purdue University, West Lafayette, IN 47907, USA

[c]Center for Implantable Devices, Purdue University, West Lafayette, IN 47907, USA

[d]School of Mechanical Engineering, Purdue University, West Lafayette, IN 47907, USA

[e]Ray W. Herrick Laboratories, Purdue University, West Lafayette, IN 47907, USA

[f]College of Veterinary Medicine, Purdue University, West Lafayette, IN 47907, USA

[g]Goodman Campbell Brain and Spine Department of Neurological Surgery Indiana University, Indianapolis, IN 46202, USA

[h]Department of Electrical and Computer Engineering Nanoscience Institute for Medical and Engineering Technologies University of Florida, Gainesville, FL 32611, USA

Abstract

Here we report on the development of polyimide-based flexible magnetic actuators for actively combating biofouling that occurs in many chronically implanted devices. The thin-film flexible devices are microfabricated and integrated into a single-pore silicone catheter to demonstrate a proof-of-concept for a self-clearing smart catheter. The static and dynamic mechanical responses of the thin-film magnetic microdevices were quantitatively measured and compared to theoretical values. The mechanical fatigue properties of these polyimide-based microdevices were also characterized up to 300 million cycles. Finally, the biofouling removal capabilities of magnetically powered microdevices were demonstrated using bovine serum albumin and bioconjugated microbeads. Our results indicate that these thin-film microdevices are capable of significantly reducing the amount of biofouling. At the same time, we demonstrated that these microdevices are mechanically robust enough to withstand a large number of actuation cycles during its chronic implantation.

Keywords

Biofouling; Magnetic microactuators; Polyimide; Thin-film device; Implantable microdevice

*Corresponding author at: Weldon School of Biomedical Engineering, Purdue University, 206 S. Martin Jischke Dr., West Lafayette, IN 47907, USA. hwlee@purdue.edu (H. Lee).

Appendix A. Supplementary data

Supplementary data associated with this article can be found, in the online version, at https://doi.org/10.1016/j.snb.2018.07.044.

1. Introduction

Biofouling is a serious issue with enormous implications for devices used in biomedical, maritime, and environmental applications [1]. For devices that chronically interface with the body, biofouling can have a detrimental impact on device performance [2]. Implantable devices such as catheters and biosensors, often suffer from catastrophic functional degradation over the course of their lifetime due to biofouling [3]. An example of biofouling related failure that can lead to critical injury for patients can be found in shunt systems used for hydrocephalus. Hydrocephalus is a neurological disorder that is characterized by an abnormal accumulation of cerebrospinal fluid (CSF) in the brain, often due to an imbalance between the generation and absorption of CSF. It is commonly diagnosed in children with approximately 1–2 newborns diagnosed for every 1000 in the United States [4,5]. Unfortunately, there is no cure for this debilitating disease. The gold standard for the treatment of hydrocephalus is the implantation of a shunt system to divert excess CSF from the brain to another part of the body [6]. As such, a sudden failure in this important device can lead to significant and rapid health decline for the patient. Unfortunately, shunt systems are notorious for their extremely high failure rate of more than 40% within 1 year and up to 85% within 10 years of implantation [7,8]. A large portion of this high failure rate can be attributed to biofouling-related obstruction and infection [7,9].

A significant amount of research effort has been devoted to mitigating such biofouling-related device failures by preventing and minimizing the attachment of biomolecules onto a surface of interest. Most anti-biofouling strategies can be classified as either passive or active methods. The passive approaches aim to prevent biofilm accumulation by creating a ‘stealth surface’, which ideally remains undetected in a biological milieu and therefore is not prone to biofouling [10]. Typically, these anti-biofouling surfaces are created using polymer coatings to decrease the interfacial energy between the surface with the surrounding solution or to reduce the intermolecular forces between the surface and the biomolecules [10]. Examples of anti-biofouling polymers include polyethylene glycol (PEG) terminated polymers [11,12], perfluoropolyether-based random terpolymers [13], zwitterionic polymers [14,15] and phosphazene polymers [16]. More recently, biomimetic micro and nanoscale patterns have also been explored to prevent biofouling. Pogodin et al., demonstrated the antimicrobial properties of nanopillar structures found on the wings of a Cicada [17]. Zhang et al., used hybrid organic–inorganic nanoflowers with silver nanoparticles to demonstrate antimicrobial activity against Gram-negative *E. coli* [18]. Moreover, Chung et al., recently engineered micro-topography found on shark skin that were shown to disrupt biofilm formation [19].

While passive anti-biofouling surfaces may decrease the rate of biofilm accumulation, they do not eliminate bio-accumulation entirely. Thus, active anti-biofouling approaches that can periodically remove, reduce or dislodge a biofilm on demand remain more attractive, especially for chronic applications (e.g., implantable devices, marine sensors, etc.). Several different electro-mechanical transducers have already been proposed for anti-biofouling applications including electrostatic repulsion, electroosmotic forces, and ultrasound-induced shear forces to combat against proteins [20], bacteria [18,21], and even blood clots [22]. Although these active methods demonstrate exciting potential for combating biofouling, they

pose challenges for chronically implantable devices because of their complexity and high power requirements.

To combat biofouling *in situ* without the morbidity, mortality, and expense of additional surgical intervention, we have previously proposed to use microfabricated magnetic actuators for removing bio-accumulation on ventricular catheters [23]. A magnetic microactuator is ideal for such applications due to its simplicity (i.e., they do not require integrated circuits or power source). In the presence of externally applied magnetic field, the microactuator torques out-of-plane to align itself to the direction of the magnetic field (Fig. 1). The amount of out-of-plane deflection can be controlled by changing the amplitude of the magnetic field and in a time-varying magnetic field, the device can move at high speed to create large shear force across its surface to remove biofouling.

Although the cellular removal capabilities [23], durability [24], and magnetic resonance imaging compatibility [25] of these devices have previously been demonstrated, they have only been fabricated on a rigid silicon substrate thus far, which complicates their integration into flexible devices. To facilitate the integration of microfabricated devices into silicone-based catheters, we designed, fabricated, and tested novel thin-film polymer-based magnetic microactuators in an effort to create a self-clearing smart catheter. In this work, we demonstrate the new process flow to create polyimide-based magnetic microactuators and integrated them into silicone-based implantable catheter for future *in vivo* evaluations. We report static and dynamic mechanical responses of these devices, as well as their mechanical stability over long-term actuation. To demonstrate anti-biofouling properties of these thin-film-based magnetic microactuators, we evaluated the impact of actuation using fluorescent protein and light-activated microbeads.

2. Experimental

2.1. Microfabrication

The process flow for the fabrication of polyimide-based magnetic microactuators has previously been described in detail [26]. Starting with a 100-mm single crystal silicon wafer (Silicon Quest, San Jose, CA), a 500-nm-thick silicon dioxide was deposited using plasma enhanced chemical vapor deposition as a sacrificial layer to facilitate the device release. On top of the oxide release layer, 12-μm-thick polyimide layer (PI-2525, HD Microsystem, Parlin, NJ) was spun on and cured as suggested by manufacturer. Next, a conduction layer of chromium (20 nm) and gold (50 nm) was evaporated (Airco E-Beam Evaporator, Livermore, CA) to facilitate the subsequent electroplating step. Nickel ferromagnetic elements (10-μm-thick) were electroplated on photolithographically-defined plating-mold using the procedure described in [24]. The structural plate was then defined using oxygen plasma etching (Advanced Oxide Etcher, Surface Technology System, Newport, UK). To release the microactuators, the wafer was placed in buffered oxide etchant for 12 h to remove the sacrificial oxide layer. After release, 500-nm-thick Parylene C layer was conformally deposited (PDS2010, Specialty Coating System, Indianapolis, IN) to improve biocompatibility.

2.2. Mechanical evaluations

To characterize the static mechanical response of the fabricated magnetic microactuator, the angular deflection as a function of the applied magnetic field strength was measured for each device. The magnetic field was generated using a bespoke iron core electromagnet. The magnetic field strength was measured using a gaussmeter (8010 Gauss, Pacific Scientific, Chandler, AZ) as a function of applied current. The individual device structure, was aligned and gently placed on a 5 mm thick PDMS mold with 2-mm-diameter through-holes for structural support Fig. 1b and c. PDMS was then placed on top of the electromagnet under a digital microscope (KH8700, Hirox, Hackensack, NJ). The top edge of the nickel magnet and the base of the cantilever were focused upon and their vertical positions were recorded. The difference between the two points was then converted into deflection angle.

The dynamic responses of the polyimide-based magnetic microactuators were measured in air and in deionized water to identify the resonant frequency at which the device actuates with high energy efficiency. An electromagnet with a 6-inch-long ferrite 77 core (Fair-Rite, Wallkill, NY) was made for measuring the dynamic responses because of its high relative permeability and excellent frequency response. The test sample was placed on a PDMS fixture on top of the electromagnet in the same manner as with the DC measurements (Fig. 1c). A scanning laser Doppler vibrometer (MSA-400, Polytec, Waldbronn, Germany) was used to measure the out-of-plane velocity at a series of points across the actuator surface. The electromagnet was driven with a swept sine excitation generated by the MSA-400 system. The fast Fourier transform algorithm was applied to the time series velocity data, and frequencydomain integration was used to develop a spatially averaged displacement spectrum for the device. A linear approximation of the impedance of the magnet was used to estimate the current applied. The H1 frequency response estimator (amplitude per unit actuation current) was then calculated, giving the best linear estimate of the relation between current and displacement from 1.25 to 1200 Hz with a 1.25 Hz resolution.

2.3. Fatigue evaluation

Each test sample was suspended on top of two thin PDMS anchor points covalently bonded on a glass slide to allow the actuator to deflect up or down during actuation. The test fixture was then placed in a small beaker filled with 1X PBS (Invitrogen, Thermo Fisher Scientific). The temperature of the PBS was maintained at 37 °C by circulating solution between a flask sitting on top of a hotplate and small beaker via a peristaltic pump. The actuators were driven at 26.5 kA/m using a 100 Hz sine wave with the same electromagnet described in preceding section. The magnet was water cooled using a separate circulating flow system. Each sample was periodically taken out of the testing setup at 300 K, 3 M, 30 M, 150 M and 300 M cycles to measure its resonant frequency in air using the LDV.

2.4. Fluid–structure interaction

A simplified numerical analysis of fluid–structure interaction of our magnetic microactuators were performed using COMSOL Multiphysics finite element modeling software (v3.5, COMSOL, Inc., Los Angeles, CA, USA). The incompressible Navier–Stokes application mode in COMSOL was used to solve Eq. (5). As discussed earlier, Stokes flow was assumed, and a series of steady-state simulations was carried out at different angular

deflection positions of the magnetic microactuators. For 2D analysis of our magnetic microactuator, a total of 18 steady-state analyses of different angular deflections of our magnetic microactuators were performed to simulate a full actuation cycle.

The simulation parameters for the 2D analyses are listed in Supplementary Table 1. The meshed model of the device at 0° deflection is shown in Supplementary Fig. 3. To simulate the continuous flow of CSF, the inlet boundary was set at 2 kPa, which is the upper limit of the normal range of the intracranial pressure; the outlet pressure was set at 0 Pa. The time-variant instantaneous velocity of the magnetic microactuator was set with the maximum velocity $v_O = D\omega_f$ at the tip of the structural plate and decreasing linearly towards the axis of rotation.

2.5. Preparation of ASBA-microbead

ASBA solution was prepared in a dark room to protect the photoactive group. In an orange light-proof bottle, we added 100 μL of dried DMSO (Thermo Scientific, Rockford, IL, USA) to 3 mg of ASBA (Thermo Scientific, Rockford, IL, USA) to make 120 mM stock solution. We then diluted the 6 μL of stock solution with 94 μL PBS to make 6 mM ASBA solution to be used for conjugation. We washed 4 mL of carboxylated 10-μm-diameter carboxylated polystyrene beads (CPX-100-10, Spherotech, Inc., Lake Forest, IL, USA) with 5 mL of 2-(*N*-morpholino) ethanesulfonic acid (MES) buffer by spinning at 3000 rcf for 4 min and resuspending the beads in fresh buffer. Next, 100 mg of EDC (Thermo Scientific, Rockford, IL, USA) and 100 mg of Sulfo-NHS (Thermo Scientific, Rockford, IL, USA) was added to microbead suspension and allowed to react in room temperature for 15 min. The reacted microbeads were washed three times with 5 mL of MES as described previously. We then added 100 μL of the previously prepared 6.0 mM ASBA solution in a dark room and allowed to react for 4 h with mixing. After the reaction, the microbeads were again washed with MES and resuspended in MES to achieve bead density of 10×10^6 beads/mL.

2.6. Jet impingement

Polyimide-coated glass microscope slides (A-1460/L, Becton, Dickonson and Company, Franklin Lakes, NJ, USA) were used as the substrate for the jet impingement experiment. The glass-slides were treated with 4 wt.% diethylenetriamine to introduce amine groups on surface [27]. The jet impingement experiment setup is shown in Fig. 4a. A 12-ml syringe (Kendall Monojet, Covidien, Mansfield, MA, USA), filled with PBS, was placed inside a linear syringe pump (PHD 2000 Infusion, Harvard Apparatus, Holiston, MA, USA). A 23-gauge needle (5123-1-B, EFD, Inc., East Providence, RI, USA) was attached to the syringe and placed on a vertical micrometer to deliver the stream of microjet. A 100 μL of the solution containing 10^6 beads per ml and 200 μL of PBS buffer was loaded onto three 1 cm^2 squares drawn on glass slides. The loaded glass slides were placed inside a quarts petri dish and placed under a long UV light for 30 min. Following UV irradiation, the petri dish containing the parylene glass slides were placed on an optical stage with vertical actuator. The needle was brought down to the glass slide surface using the vertical micrometer and positioned perpendicularly at a height equal to two times the inner diameter of the availability needle. The flow rate of microjet was calculate to deliver the fluid at $Re = 1000$

for 5 s. For each square centimeter area, as many as 25 non-lesions legions were created depending on the lesion size.

2.7. Circulating biofouling model

To ensure that the microbeads have robust attachments to the microactuator surface, 50 mM of ASBA concentration was used during the conjugation step. To accelerate the occlusion process, a concentration of 6×10^5 microbeads per mL was used, which is approximately 10 times higher than what has previously been used in a similar experiment [28]. The microbead reservoir solution was made with 15 million ASBA-conjugated microbeads and 15 million amine-conjugated microbeads in 50 mL MES. The prepared microbead solution was placed in a lightproof 75-mL cell-culture flask and mixed continuously using a magnetic stir plate and flowed through the system at 0.75 mL/min, which corresponds to the upper range of human CSF production rate [29,30]. A self-clearing catheter sample was placed into an interconnect apparatus with custom-made PDMS gaskets. Once the fluidic component of the circulating occlusion system was running, the fluorescent source was turned on and the UV light filter was placed to photoactivate the ASBA-functionalized microbeads as it travels through the pores at 30-s intervals to monitor the occlusion progress. Once the device was determined to be occluded the time-lapse interval was reduced to 1-s to capture the occlusion clearing process. To activate the magnetic microactuator, an ac magnetic field with 30 kA/m and 10 Hz was applied using a signal generator and a power supply for 1 min.

3. Results

3.1. Mechanical evaluations

Our thin film devices share the same cantilever-based design fabricated on bulk silicon wafers [24,25]. Here we used a uniform polyimide layer as the structural base to facilitate integration into soft silicone catheters. Polyimide is chosen for excellent chemical resistance, biocompatibility and favorable mechanical properties [31]. At the tip of the cantilever beam, an electroplated ferromagnetic material covers the surface of a circular structural plate (Fig. 1a and b). The diameter of the structural plate is 900 μm, slightly smaller than the pore size of a conventional catheter. In the presence of a magnetic field, the magnetic element can apply a moment on the flexure, causing out-of-plane deflection (Fig. 1c). The large amplitude out-of-plane deflections produced in this manner can remove biofouling. Once released, the thin-film magnetic microactuator stays below the pore surface (Fig. 1d and e). Assuming that the load on the polyimide cantilever is a concentrated on its tip, the relationship between the applied magnetic field and the resulting deflection angle ϕ can be described by $\phi = V_{\mathrm{m}}\mathrm{MHsin}\left(\frac{\pi}{2} - \phi\right)/k_{\mathrm{beam}}$ with cantilever stiffness k_{beam}, magnet volume V_{m}, magnetization M, and applied magnetic field H (Fig. 1c) [32,33]. We have experimentally determined 12 μm as the optimal thickness for reasonable stiffness and overall structural strength [26]. With the fixed thickness, we varied the cantilever beam length (250–500 μm)and width (40–50 μm) to optimize device performance. To demonstrate a proof-of-concept microelectromechanical systemsenabled self-clearing catheter, we integrated our device into a silicone catheter in a similar fashion as described by Li et al. (Fig. 1e) [34].

Our device structure was manually slid inside a catheter and aligned to the hole punctured in a central venous access device (Cook Model G0664), which has the inner diameter of ~800 μm. The polyimide substrate was rolled to comply with catheter wall curvature and fixed in place with silicone adhesive.

Fig. 2a shows the static responses of fabricated devices. As the amplitude of the applied magnetic field increase, the out-of-plane deflection increased approaching nearly 70°. Our results indicate that approximately 15–25 kA/m of magnetic field strength can result in fairly large deflections (> 45°), and this will serve as a general guide to what magnetic field strength is needed to actuate the device *in vivo*. To evaluate dynamic behavior, our magnetic microactuator was modeled as a cantilever–tip mass system. The resonant frequency can be approximated by solving the natural modes of free vibration. According to Euler–Bernoulli theory [35], free transverse vibration of a thin uniform cantilever can be described by:

$$\frac{\mathrm{EI}}{\rho A}\frac{\partial^4 W(x,t)}{\partial x^4}+\frac{\partial^2 W(x,t)}{\partial t^2}=0, \tag{1}$$

where $W(x, t)$ is vertical deflection amplitude as a function of length and time t, at position x along length of the beam. A, I, ρ, E, are the cross section area, the second moment of inertia, density, and the Young's modulus of beam, respectively. The natural vibration frequency $\omega = 2\pi f$ can be solved by applying proper boundary conditions to $W(x, t)$. In our case, the cantilever is fixed at base at all time, therefore:

$$W(0,t)=0;\frac{\mathrm{dW}(0,\ t)}{\mathrm{dx}}=0. \tag{2}$$

On the other end of cantilever ($x = L$), the shear force must match with the tip mass m:

$$\mathrm{EI}\frac{\partial^3 W(L,t)}{\partial x^3}=m\frac{\partial^2 W(L,t)}{\partial t^2}. \tag{3}$$

Tip mass m is defined as the mass of structural plate plus the nickel on top. The bending moment at $x = L$ must also match with the moment of inertia of tip mass J:

$$\mathrm{EI}\frac{\partial^2 W(L,t)}{\partial x^2}=-J\frac{\partial^3 W(L,t)}{\partial x\,\partial t^2}. \tag{4}$$

The moment of inertia J is calculated from the geometry of structural plate. The primary flexural resonant frequency is solved for numerically after applying boundary conditions (2), (3), (4) to Eq. (1). Fig. 2b shows the plot of H1 frequency response of a sample device in both air and in water. When submerged, the primary mode resonant frequency decreased considerably from ~450 Hz to ~100 Hz. Compared to expected value, the measured resonant frequency was lower by approximately 3% (Table 1). We suspect that this discrepancy between the observed resonant frequency in air and the theoretical prediction may be due to

a small variation in fabrication results (i.e., beam geometry and electroplated nickel thickness).

Since it is important to ensure that these polyimide-based microactuators are strong enough to survive extended cycles of actuation *in vivo*, we examined the mechanical fatigue property of our microdevices. Each sample was continuously actuated for > 300 million cycles, which roughly equates to approximately 30 years of lifetime for 30-min of weekly actuation. We expected to demonstrate changes in mechanical integrity of each device by monitoring their resonant frequency. Fig. 2c shows percent change in resonant frequency from cycle 1 to 300 million. The resonant frequency shifts at the end of 300 million cycles compared to the initial state ranged between −4.3 and 3.2% (Fig. 2d). At the end of 300 M cycles, no sample exhibited any changes in polymer geometry in terms of swelling or shrinkage as expected. There were also no visible cracks or dents on any of the test samples. However, all samples exhibited some form of salt deposit likely due to extended submersion in phosphate buffered saline (PBS), which may have contributed to changes in resonant frequency (Fig. 2e).

3.2. Fluid–structure interaction

Understanding the dynamic responses in fluid is critical in designing implantable magnetic microactuators that are effective against biofouling. As noted previously, the dynamics of microactuator changes drastically when device is submerged in liquid due to effects of damping (Fig. 2b). Although there are several examples of analytical solutions used to predict the dynamic responses of cantilever beams in viscous fluids [36–39], many are limited to constant-width microactuators with small deflection amplitude, which does not reflect our design with circular structural plate and ferromagnet. Thus, here we used numerical analysis to evaluate the fluid–structure interaction.

Our hypothesis is that the movement of magnetic microactuator, which is surrounded by CSF, produces significant amount of shear stress to physically remove adsorbed biofouling material. Therefore, characterizing the shear stress distribution across the surface of our magnetic microactuators as it moves in a continuous flow may provide additional insight on optimizing device design. The shear stress τ responsible for removing cells on the device surface is related to the fluid velocity by $\tau = \mu \partial u / \partial y$, with the dynamic viscosity of the fluid μ and the fluid velocity gradient $\partial u / \partial y$.

The CSF contains a mixture of protein and cellular material, which may suggest a complex non-Newtonian fluidic behavior. However, past investigations on the fluid mechanical properties of CSF have shown that, even at an elevated level of proteins and cells, CSF behaves like a Newtonian fluid in which the shear stress and the applied strain have a linear relationship [40–42]. In addition, it is common to treat CSF as an incompressible viscous fluid as evidenced by several CSF computational fluid dynamic studies [43–46]. The motion of an oscillating solid body immersed in viscous fluid for an incompressible fluid where $\nabla \cdot \upsilon = 0$, can be described with a simplified Navier–Stokes equation [47]

$$\rho\left(\frac{\partial v}{\partial t}\right) + v \cdot (\nabla v) = -\nabla p + \mu \Delta v, \quad (5)$$

with fluid density ρ, fluid velocity v, and volume viscosity μ. In cases of low actuation frequency and hence low fluid velocity (i.e., $Re < 1$), Eq. (5) may be further simplified to ignore inertial effects and the velocity profile of the fluid may be assumed to be steady at any point in time, giving

$$0 = (-\nabla p) + \mu \Delta v. \quad (6)$$

The kinematic Reynolds number Re for the flow generated by the oscillating body can be written as $Re = \omega D^2/\nu$, with the characteristic length of the oscillating body D and the kinematic viscosity of the fluid $\nu = \rho/\mu$. The Reynolds number for our devices actuating at its primary resonance in fluid (~100 Hz) is approximately 46, which is beyond the typical conditions of Stokes flow in which the inertial effects can be ignored. However, there are examples in literature of employing the assumption of Stokes flow for microscale devices with $28 < Re < 67$ [48,49,46]. For the analyses of our magnetic microactuators, we assumed slower actuation frequency (10 Hz) to justify Stokes flow and to simplify the fluidic model (Supplementary Table 1).

Fig. 3a illustrates the fluidic motions caused by our magnetic microactuator moving at 10 Hz. The microactuator acts as a closed-valve at $t = 0$. As the actuator rotates open against the fluidic current, the fluid velocity through the catheter pore increases until its maximum when $\omega t = \pi/2$. The magnitude of shear stress across the top surface of our device (i.e., left wall of the moving boundary) was quantified. Fig. 3b illustrates different shear stress profiles of our microactuators at various angular deflection states. As expected, the results indicate that as the angular deflection of the device increases, so does the shear stress across its surface. In Supplementary Table 2, we reviewed the adhesion properties of several different biofouling materials and found that, in general, a shear stress of > 2.5 kdyn/cm^2 will remove most surface-bound cells. From Fig. 3c, we can see that the device can certainly generate high enough shear stress to remove the cellular occlusion above a certain angular deflection level. Specifically, we can expect nearly 40% of our microactuator surface to experience a shear stress that exceeds 2.5 kdyn/cm^2 when the device is deflected 60° with 40 kA/ m of applied magnetic field (Fig. 2a). This shear stress results are encouraging because we may expect to see a greater shear stress by actuating the device at a higher frequency while maintaining similarly large deflection.

3.3. Circulating biofouling model using cellular analogue

To better recapitulate the dynamic CSF flow through the smart catheter, we created a circulating biofouling model with bioconjugated cellular analogue. The idea is to create a cellular analogue that will aggressively adhere to the magnetic microactuators within hours and to provide a platform for evaluating performance of our devices in a dynamic fluid environment. Although there are examples of circulating bioreactors that may be used [28],

it is difficult to mimic robust biofouling that occurs *in vivo* due to difficulty in maintaining cell culture sterility over long-term.

Here we conjugated 10-μm polystyrene microbeads (CFP-10056-2, Spherotech, Inc. Lake Forest, IL, USA) with photoactivated crosslinker, 4-p-azidosalicylamido-butylamine (ASBA, Thermo Scientific, Rockford, IL, USA) to create cellular analogue. ASBA has an amine group on one end and a phenylazide group on the other end [50]. The amine functional group can be used to attach the crosslinker onto the carboxylic acid functional groups on polystyrene microbeads by using a well-recognized conjugation chemistry with *N*-hydroxy-sulfosuccinimide (Sulfo-NHS, Thermo Scientific) and 1-ethyl-3-[3-dimethylaminopropyl] carbodiimide hydrochloride (EDC, Thermo Scientific, Supplementary Fig. 1). The photosensitive phenylazide releases N_2 upon photoactivation by long ultraviolet light (315–410 nm) and becomes a nitrene which can bind to amine functional groups. Using ASBA linker as an analogue for the cell-adhesion molecules have several advantages. Since photoactivated ASBA on the microbeads will attack free amine groups, no additional immobilization steps are needed on the target surface.

To quantify the adhesion strength of the ASBA-conjugated polystyrene microbeads, we used simple jet impingement technique (Fig. 4a), which takes advantage of the shear stress gradient that occurs when a submerged stream of microjet impinges against a planar surface [51]. The shear force peaks at a position just outside of the microjet radius and decreases as a function of radial distance away from the axis. It is then possible to estimate the shear stress needed to remove microbeads from the surface by measuring the radius of lesion created by the microjet impinging upon a layer of microbeads (Fig. 4b). With only 6 mM of ASBA, the average detachment shear stress ranged from 615 to 669 dyn/cm^2. When conjugated with more than 25 mM of ASBA, the shear stress increased to 1981 dyn/cm^2. Moreover, when ABSA-conjugated microbeads were mixed with NH_2-microbeads, the detachment shear stress increased statistically significantly ($p < 0.01$, Fig. 4c). This may be due to additional availability of nucleophilic species, which can promote a more robust cross-linking between ASBA-conjugated and NH_2-conjugated microbeads.

The circulating biofouling setup allows wide-view optical access to an array of devices in a dynamic fluidic environment (Fig. 4d). It features three main components: an inverted microscope (Olympus CKX41SF, Olympus America, Inc., Center Valley, PA, USA) equipped with a CCD camera (Orca-Flash2.8, Hamamatsu Photonics, K. K., Hamamatsu City, Japan) and a computer with image-analysis software (MetaMorph TL, Molecular Devices, Sunnyvale, CA, USA), a custom electromagnet driven by a signal generator and a power supply, and a fluidic circuit with a reservoir containing the chemically modified microbeads. The fluidic circuit driven by a peristaltic pump featured a custom-fabricated device-interface apparatus that allows the microbead containing solution to flow through the catheter pore.

After 11 h of continuous flow using the experimental parameter described below, the microactuators were determined to be fully occluded. Supplementary Fig. 2 shows the progression of microactuator occlusion. Qualitatively, we observed most occlusion occurred within the first 6 h. With the image-processing software, we quantified the number of pixels

in each image that exceeds an intensity threshold. Fig. 4e demonstrates the occlusion clearing capability of the magnetic microactuators. The normalized patency was plotted versus time throughout the occlusion and recanalization steps (Fig. 4f). The baseline patency at the end of occlusion process prior to actuation was ~10%. Following the actuation protocol, the patency of the pore is restored back to ~95%, which demonstrates robust occlusion clearing capability of the magnetic microactuator. The mixture of ASBA + NH_2 microbeads required ~2.7 kdyn/cm^2 of shear stress to detach Fig. 4c. The fact that our device showed more than 90% patency restoration suggest that our device is capable of exerting greater forces when driven at a higher actuation frequency (40 Hz).

3.4. Protein removal

When a device is implanted in the body, a thin proteinaceous layer forms on its surface, which facilitates an immune hypersensitivity reaction by allowing formation of Arginine–Glycine–Aspartic (RGD) acid receptor–ligand complexes that recruits more inflammatory cells to the device surface [52–54]. RGD peptide is a part of recognition sites of a transmembrane protein, integrin, that mediates cellular adhesion to its surrounding extracellular matrix [55]. The integrin-RGD interaction is also known to play a role in cellular mechanotransduction, which is important in cell survival and growth [56,57]. If it is possible to prevent protein layer formation, it may be possible to delay or prevent downstream inflammatory reaction that result in capsule formation [3].

To characterize the protein-based biofouling removal capability of polyimide-based thin-film magnetic microactuators, we coated our devices using fluorescent-tagged bovine serum proteins (BSA-FITC, ThermoFisher Scientific, Waltham, MA, USA). The shear stress required to remove BSA has previously been reported to be in the order of 1–10 dyn/cm^2 [58,59]. As such, we expected our microactuators to have little trouble in removing the adsorbed BSA-FITC. The fluorescence intensity of absorbed BSA-FITC plateaued around 5 mg/ml on Parylene surface, therefore, all BSA-FITC evaluations used this concentration. Each sample was placed inside a sterile test tube with 5 mg/mL of BSA-FITC in PBS and incubated for 2 h. The images of protein coated samples ($n = 8$) were taken using a fluorescence microscope (Axio Observer Z1, Carl Zeiss Microscopy, LLC) using filter set 17 (excitation, BP 485/20, and emission BP 515–565, Carl Zeiss Microscopy, LLC). Next, we investigated the impact of actuation of our microdevices on adsorbed protein concentration. Four protein-coated microactuators were subjected to 26.5 kA/m of magnetic field at 40 Hz for 5 min, and re-imaged. A set of control devices ($n = 4$) was treated with 5 min of zero magnetic field. The fluorescence intensity of microactuator surfaces before and after actuation was quantified using imageJ software (version 1.50i). Fig. 5a–d shows fluorescence images of BSA-FITC coated microactuators. Without actuation, little change in fluorescence intensity was observed. However, actuated samples show statistically significant reduction in fluorescence ($p < 0.01$), which suggests robust biofouling removal.

4. Conclusions and discussion

Here we report on the development of polyimide-based thin-film magnetic microactuator, which exhibits great promise for combating protein-based biofilm accumulation. Preventing

protein adsorption on device surface is thought to delay the inflammatory response because macrophages bind to specific regions of fibrinogen and albumin that immediate passivate the implant surface [3,60]. Similarly, implanted ventricular catheters are also known to be covered in albumin [61]. The overarching goal of our work is to use our microfabricated devices to prophylactically remove the potential binding sites of macrophages and prevent formation of fibrous capsule around the implant. The periodic actuation may be performed as an inpatient procedure during which a custom electromagnet can be used to locally apply external magnetic field over the implant.

We found that the flexible nature of our microfabricated devices facilitates the integration with into an implantable catheter (Fig. 1). The manual integration of our single device was relatively simple and straightforward, although we suspect that alignment of an array of device in a multi-pore catheter design may be more challenging. Nevertheless, it may not be necessary to have each inlet pores be integrated with a magnetic microactuator since the biofouling-related occlusion occurs most often on the proximal inlet pores where the flow rate is the highest [62,63]. Therefore, it may be possible to vary the number and location of devices to optimize catheter performance.

The mechanical responses of these microfabricated devices showed good agreement with theoretical values, which indicates adequate control of our fabrication processes. The static deflection of magnetic microactuator mirrored the expected value closely and the resonant frequency of our microactuators differed on average by less than 4% (Fig. 2a and b). To mitigate potential device failure due to chronic actuation, we evaluated the shift in resonant frequency following over 300 million cycles of actuation, which corresponds to more than 30 years of lifetime for 30-min of weekly actuation at 100 Hz. The change in resonant frequency was also relatively minor with the maximum change being approximately 4.3%. Our post-actuation examination showed that all tested samples showed deposition of salt crystals which could have contributed to the shift in resonant frequency (Fig. 2e). Overall, the polyimide-based magnetic microactuators were demonstrated to be flexible enough for simple integration into an implantable catheter and mechanically robust enough to be chronically implanted.

To better understand the mechanism of our active anti-biofouling devices, we performed a numerical analysis to model the fluid–structure interaction (Fig. 3). As the actuator sweeps across the inlet pore surface, the increased flow rate causes an elevation of shear stress across device surface, which can exceed adhesion strength of various biofouling materials (Supplementary Table 2). We noted that increasing the amplitude of actuation can increase the microactuator surface area that exceed certain detachment strength. Although a more sophisticated simulation may be required to assess the impact of inertial effects and higher actuation speeds, our results corresponds well with subsequent experimental results to suggest that this simple analysis may be used to facilitate future device design.

We also reported on the development of a circulating-flow biofouling test platform using cellular analogue. The presented test-platform subjects self-clearing catheters under a more realistic dynamic fluid environment found in *in vivo*. We have found that the ASBA-conjugated microbeads serves as a robust cellular substitute that can expedite the occlusion

process without significant efforts to maintain viable cell culture over time. These cellular analogues have been shown to feature comparable adhesion strength as some fibroblasts (Supplementary Table 2). Using an inverted fluorescent microscope, we were able to visualize the occlusion and self-clearing processes of anti-biofouling catheter. With this test platform, we demonstrated that our magnetic microactuators can be activated in a continuously flowing environment to remove accumulated obstruction (Fig. 4). Although the polystyrene microbeads do not recapitulate the complex cell-cell and cell-matrix interaction that can significantly effect the biofouling-removal capabilities of these microactuators, this simplified evaluation method may increase the experimental throughput necessary to optimize device design.

Finally, we demonstrated the capability of our devices to expel protein layer that adhered to its surface (Fig. 5). Inflammatory processes often begin with proteinaceous layer formation that triggers recruitment of macrophages [3]. By periodically removing protein coating that occurs following implantation, it may be possible to delay the inflammatory response that can leads to a premature implant failure. Compared to the control devices, the amount of albumin reduction exceed more than 90% with only 5 min of actuation. Indeed, there are several other plasma proteins that can trigger inflammatory response including fibrinogen (340 kDa) and fibronectin (220 kDa) that have different molecular weights than albumin (66.5 kDa). However, the non-specific interaction is mainly affected by the hydrogen bonding as well as the hydrophobic, Van der Waals, electrostatic, and macromolecular forces, and thus more sensitive to the isoelectric points (pI) of each protein [64,65]. Although additional experiments will be needed, our hypothesis is that these other proteins will feature similar adhesion properties that can be overcome by our microactuators since they all have similar isoelectric points (pI = 5.5 for fibrinogen and fibronectin and pI = 4.7 for albumin) [66–69]. Therefore, we believe our result provides the preliminary evidence to suggest that these self-clearing catheters can not only be used to remove cellular biofouling [23], but may also be used to combat protein film growth that precedes macrophage recruitment.

Despite our promising results, additional experiments are needed to fully characterize the anti-biofouling capacity of magnetic microactuators. As previously mentioned, biofouling refers to a wide scale of biological materials including proteins, bacteria, cells, and tissue. Although this work focused on characterization of mechanical shear generated by the magnetic microactuator motion and its capacity to remove non-specifically adsorbed protein, additional work is necessary to quantify the impact of microactuation on combating bacterial biofilm since a large percentage of implanted devices also suffer from bacterial infection-related failures [70]. Our hypothesis is that prophylactic removal of protein can also prevent bacterial accumulation since fibrinogen, fibronectin, albumin, and collagen are known to promote microbial adhesion [71]. It may also be interesting to leverage aforementioned passive anti-biofouling approaches [17–19] in combination with our active actuation platform to further improve biofilm prevention and reduction.

Another potential caveat to our anti-biofouling approach is that it is not clear what happens to the displaced biomaterial. Understanding the downstream impact of removed biomaterials will be important in clinical utility of these devices. The ultimate aim of this research is to

utilize these smart self-clearing implantable devices to improve the reliability and lifetime of implantable devices by preventing and removing biofouling. The reported results further demonstrate the proof-of-concept of using active mechanisms to combat biofouling in a more physiologically relevant test environment against various biofouling materials. In the future, however, we will evaluate the performance of our devices *in vivo* to demonstrate that our smart catheter can combat biofouling in a more complex environment without adverse effects.

Supplementary Material

Refer to Web version on PubMed Central for supplementary material.

Acknowledgments

This work was supported NIH NINDS (R21NS062324 and R21NS095287) and NIH/NCRR Indiana CTSI (UL1TR001108). The authors would like to thank Cook Medical for providing a sample central venous access devices (Model G0664).

Biography

Qi Yang received his B.S. in Electrical and Computer Engineering in 2014 from Purdue University. He is now working towards his Ph.D. in Electrical Engineering at Purdue. His current research interests include bioMEMS devices, biosensors, and implantable devices.

Hyunsu Park received his B.S. in Chemical and Biomolecular Engineering from Sogang University in 2014. He received an M.S. in Materials Science and Engineering from KAIST in 2015. He is currently working towards his Ph.D. in Biomedical Engineering at Purdue. He is interested in biology and fabrication of MEMS devices for biomedical application.

Tran Nguyen received her B.S. in Chemical Biology from University of California, Berkeley in 2013. She is now working towards her Ph.D. in Biomedical Engineering at Purdue University. Her current research interests include implantable biochemical sensors.

Jeffrey F. Rhoads is a Professor in the School of Mechanical Engineering at Purdue University and is affiliated with both the Birck Nanotechnology Center and Ray W. Herrick Laboratories at the same institution. He also serves as the Director of Practice for MEERCat Purdue: The Mechanical Engineering Education Research Center at Purdue University. Dr. Rhoads received his B.S., M.S., and Ph.D. degrees, each in mechanical engineering, from Michigan State University in 2002, 2004, and 2007, respectively. Dr. Rhoads' current research interests include resonant micro/nanoelectromechanical systems; energetic materials (including explosives, pyrotechnics, and propellants); additive manufacturing; and mechanics education.

Dr. Albert Lee is a practicing neurosurgeon in the Department of Neurological Surgery, Indiana University School of Medicine. He graduated with B.S. and M.S. in electrical engineering from Georgia Institute of Technology in 1999 and 2000, respectively. He then went on to receive his M.D. from St. George's University in 2005. He completed Neurological Surgery residency in 2012 at University of Texas, Southwestern and his

fellowship in Neurological Surgery in 2013 from Oregon Health and Science University. Dr. Lee's research interests include pain, epilepsy, movement disorder. He also is specialized in treating hydrocephalus and medical refractory spasticity.

Dr. R. Timothy Bentley is a veterinary neurologist-neurosurgeon in the Department of Veterinary Clinical Sciences, Purdue University College of Veterinary Medicine. He graduated as a veterinarian from the University of Liverpool in 2005 and completed an internship and residency at the Royal Veterinary College, University of London and the Tufts University Cummings School of Veterinary Medicine. He was board-certified in the subspecialty of Neurology by the American College of Veterinary Medicine in 2009. His interests include brain tumors and all aspects of intracranial surgery.

Jack W. Judy received the B.S.E.E. degree (summa cum laude) from the University of Minnesota, Minneapolis, MN, USA, in 1989, and the Ph.D. and M.S. degrees from the University of California at Berkeley, Berkeley, CA, USA, in 1996 and 1994, respectively. He was with the faculty of the Electrical Engineering Department, University of California at Los Angeles, Los Angeles, CA, USA, from 1997 to 2013. From 2009 to 2013, he was a Program Manager at the Microsystems Technology Office of the Defense Advanced Research Projects Agency (DARPA). At DARPA, he initiated and managed the Reliable Neural Interface Technology Program. He is currently with the Nanoscience Institute for Medical and Engineering Technology, University of Florida, Gainesville, FL, USA. His current research interests include additional novel ferromagnetic MEMS and NEMS devices, chemical sensors, micromachined instruments for plasma research, and a variety of advanced neuroengineering projects, such as advanced neurosurgical microdevices, reliable high-density bi-directional neural-interface systems, and miniaturized high-resolution neural-imaging technologies.

Hyowon Lee is an Assistant Professor in the Weldon School of Biomedical Engineering at Purdue University and is a member of Birck Nanotechnology Center and the Center for Implantable Devices at Purdue. He received a B.A. in Neuroscience from the Colorado College in 2004, and an M.S and a Ph.D. in Biomedical Engineering from the University of California, Los Angeles, in 2008 and 2011, respectively. Dr. Lee's current research interests include chronically implantable micro/nano devices; anti-biofouling strategies; and development of safe and energy efficient neurostimulation devices.

References

[1]. Simões M, Simões LC, Vieira MJ, A review of current and emergent biofilm control strategies, LWT Food Sci. Technol 43 (4) (2010) 573–583.

[2]. Yu L, Kim B, Meng E, Chronically implanted pressure sensors: challenges and state of the field, Sensors 14 (11) (2014) 20620–20644. [PubMed: 25365461]

[3]. Ward WK, A review of the foreign-body response to subcutaneously-implanted devices: the role of macrophages and cytokines in biofouling and fibrosis, J. Diabetes Sci. Technol. (Online) 2 (5) (2008) 768–777.

[4]. Chi JH, Fullerton HJ, Gupta N, Time trends and demographics of deaths from congenital hydrocephalus in children in the United States: National Center for Health Statistics data, 1979 to 1998, J. Neurosurg. Pediatr 103 (2) (2005) 113–118.

[5]. Simons TD, Hall M, Riva-Cambrin J, Albert JE, Jeffries HE, Lafleur B, Dean JM, Kestle JRW, Network THCR, Infection rates following initial cerebrospinal fluid shunt placement across pediatric hospitals in the United States, J. Neurosurg. Pediatr 4 (2) (2010) 156–165.

[6]. Lutz BR, Venkataraman P, Browd SR, New and improved ways to treat hydrocephalus: pursuit of a smart shunt, Surg. Neurol. Int 4 (Suppl. 1) (2013) S38–50. [PubMed: 23653889]

[7]. Browd SR, Ragel BT, Gottfried ON, Kestle JRW, Failure of cerebrospinal fluid shunts: Part I: Obstruction and mechanical failure, Pediatr. Neurol 34 (2) (2006) 83–92. [PubMed: 16458818]

[8]. Harris CA, McAllister JP, What we should know about the cellular and tissue response causing catheter obstruction in the treatment of hydrocephalus, Neurosurgery 70 (6) (2012) 1589–1601 discussion 1601–2. [PubMed: 22157548]

[9]. Drake JM, Sainte-Rose C. (Eds.), The Shunt Book, Blackwell Science, Cambridge, 1995.

[10]. Krishnan S, Weinman CJ, Ober CK, Advances in polymers for anti-biofouling surfaces, J. Mater. Chem 18 (2008) 3405–3413.

[11]. Schilp S, Rosenhahn A, Pettitt ME, Bowen J, Callow ME, Callow A, Grunze M, Physicochemical properties of (ethylene glycol)-containing self-assembled monolayers relevant for protein and algal cell resistance, Langmuir 25 (16) (2009) 10077–10082. [PubMed: 19469528]

[12]. Ma H, Hyun J, Stiller P, Chilkoti A, Non-fouling oligo(ethylene glycol)-functionalized polymer brushes synthesized by surface-initiated atom transfer radical polymerization, Adv. Mater 16 (4) (2004) 338–341.

[13]. Yarbrough JC, Rolland JP, DeSimone JM, Callow ME, Finlay JA, Callow JA, Contact angle analysis, surface dynamics, and biofouling characteristics of crosslinkable, random perfluoropolyether-based graft terpolymers, Macromolecules 39 (7) (2006) 2521–2528.

[14]. Cho WK, Kong B, Choi IS, Highly efficient non-biofouling coating of zwitterionic polymers: poly((3-(methacryloylamino)propyl)-dimethyl(3-sulfopropyl)ammonium hydroxide), Langmuir 23 (10) (2007) 5678–5682. [PubMed: 17432887]

[15]. Yang Y.-f., Li Y, Li Q.-l., Wan L.-s., Xu Z.-k., Surface hydrophilization of microporous polypropylene membrane by grafting zwitterionic polymer for anti-biofouling, J. Membr. Sci 362 (1–2) (2010) 255–264.

[16]. Satzl S, Henn C, Christoph P, Kurz P, Stampfl U, Stampfl S, Thomas F, Berger I, Richter GM, The efficacy of nanoscale poly[bis(trifluoroethoxy)phosphazene] (PTFEP) coatings in reducing thrombogenicity and late in-stent stenosis in a porcine, Investig. Radiol 42 (5) (2007) 303–311. [PubMed: 17414526]

[17]. Pogodin S, Hasan J, Baulin VA, Webb HK, Truong VK, Hong T, Nguyen P, Boshkovikj V, Fluke CJ, Watson GS, Watson JA, Crawford RJ, Ivanova EP, Biophysical model of bacterial cell interactions with nanopatterned cicada wing surfaces, Biophys. J 104 (4) (2013) 835–840. [PubMed: 23442962]

[18]. Zhang M, Peltier R, Zhang M, Lu H, Bian H, Li Y, Xu Z, Shen Y, Sun H, Wang Z, In situ reduction of silver nanoparticles on hybrid polydopamine-copper phosphate nanoflowers with enhanced antimicrobial activity, J. Mater. Chem. B 5 (27) (2017) 5311–5317. [PubMed: 32264069]

[19]. Chung KK, Schumacher JF, Sampson EM, Burne RA, Antonelli PJ, Brennan, Impact of engineered surface microtopography on biofilm formation of Staphylococcus aureus, Biointerphases 2 (2007) (2016) 89–94.

[20]. Yeh P-YJ, Kizhakkedathu JN, Madden JD, Chiao M, Electric field and vibration-assisted nanomolecule desorption and anti-biofouling for biosensor applications, Colloids Surf. B: Biointerfaces 59 (1) (2007) 67–73. [PubMed: 17532612]

[21]. Poortinga AT, Smit J, Mei HCVD, Busscher HJ, Electric field induced desorption of bacteria from a conditioning film covered substratum, Biotechnol. Bioeng (2001) 395–399. [PubMed: 11745167]

[22]. Kim J, Lindsey BD, Chang W.-y., Dai X, Stavas JM, Dayton PA, Jiang X, Intravascular forward-looking ultrasound transducers for microbubble-mediated sonothrombolysis, Sci. Rep 7 (4) (2017) 1–10. [PubMed: 28127051]

[23]. Lee SA, Lee H, Pinney JR, Khialeeva E, Bergsneider M, Judy JW, Development of microfabricated magnetic actuators for removing cellular occlusion, J. Micromech. Microeng 21 (5) (2011) 054006.

[24]. Lee H, Kolahi K, Bergsneider M, Judy JW, Mechanical evaluation of un-obstructing magnetic microactuators for implantable ventricular catheters, J. Microelectromech. Syst 23 (4) (2014) 795–802. [PubMed: 29151776]

[25]. Lee H, Xu Q, Shellock FG, Bergsneider M, Judy JW, Evaluation of magnetic resonance imaging issues for implantable microfabricated magnetic actuators, Biomed. Microdevices 16 (1) (2014) 153–161. [PubMed: 24077662]

[26]. Yang Q, Nguyen T, Liu C, Miller J, Rhoads JF, Linnes J, Lee H, Polyimide-based magnetic microactuators for biofouling removal, 2016 38th Annual International Conference of the IEEE Engineering in Medicine and Biology Society (EMBC) (2016) 5757–5760.

[27]. Santoso F, Albrecht W, Schroeter M, Weigel T, Paul D, Schomacker R, A novel technique for preparation of aminated polyimide membranes with microfiltration characteristics, J. Membr. Sci 223 (1) (2003) 171–185.

[28]. Harris CA, Resau JH, Hudson EA, West RA, Moon C, McAllister II, Mechanical contributions to astrocyte adhesion using a novel in vitro model of catheter obstruction, Exp. Neurol 222 (2) (2010) 204–210. [PubMed: 20051241]

[29]. Milhorat TH, Hammock MK, Fenstermacher JD, Rall DP, Levin VA, Cerebrospinal fluid production by the choroid plexus and brain, Science 173 (1971) 330–332. [PubMed: 4997797]

[30]. Nilsson C, Stahlberg F, Thomsen C, Henriksen O, Herning M, Owman C, Circadian variation in human cerebrospinal fluid production measured by magnetic resonance imaging, Am. J. Physiol. Regul. Integr. Comp. Physiol 262 (1992) R20–R24.

[31]. Xiao SY, Che LF, Li XX, Wang YL, A novel fabrication process of MEMS devices on polyimide flexible substrates, Microelectron. Eng 85 (2) (2008) 452–457.

[32]. Roark RJ, Roark's Formulas for Stress and Strain, McGraw-Hill, New York, 1989.

[33]. Judy JW, Muller RS, Zappe HH, Magnetic microactuation of polysilicon flexure structures, J. Microelectromech. Syst 4 (4) (1995) 162–169.

[34]. Li C, Wu P-M, Han J, Ahn CH, A flexible polymer tube lab-chip integrated with microsensors for smart microcatheter, Biomed. Microdevices 10 (5) (2008) 671–679. [PubMed: 18483863]

[35]. Rao SS, Transverse Vibration of Beams, Wiley, 2007.

[36]. Sader JE, Frequency response of cantilever beams immersed in viscous fluids with applications to the atomic force microscope, J. Appl. Phys 84 (1998) 64–76.

[37]. Kirstein S, Mertesdorf M, Schdönhoff M, The influence of a viscous fluid on the vibrating dynamics of scanning near-field optical microscopy fiber probes and atomic force microscopy cantilevers, J. Appl. Phys 84 (1998) 1782–1790.

[38]. Chon JWM, Mulvaney P, Sader JE, Experimental validation of theoretical models for frequency response of atomic force microscope cantilever beams immersed in fluids, J. Appl. Phys 87 (2000) 3978–3988.

[39]. Dareing DWFT, Thundat T, Effective mass and flow patterns of fluids surrounding microcantilevers, Ultramicroscopy 106 (2006) 780–794.

[40]. Brydon HL, Hayward R, Harkness W, Bayston R, Physical properties of cerebrospinal fluid of relevance to shunt function. 1: The effect of protein upon CSF viscosity, Br. J. Neurosurg 9 (1995) 639–644. [PubMed: 8561936]

[41]. Brydon HL, Bayston R, Hayward R, Harkness W, The effect of protein and blood cells on the flow-pressure characteristics of shunts, Neurosurgery 38 (3) (1996) 498–504. [PubMed: 8837802]

[42]. Bloomfield IG, Johnston IH, Bilston LE, Effects of proteins, blood cells and glucose on the viscosity of cerebrospinal fluid, Pediatr. Neurosurg 28 (1998) 246–251. [PubMed: 9732257]

[43]. Egnor M, Rosiello A, Zheng L, A model of intracranial pulsation, Pediatr. Neurosurg 35 (2001) 284–298. [PubMed: 11786696]

[44]. Kurtcuoglu V, Poulikakos D, Ventikos Y, Computational modeling of the mechanical behavior of the cerebrospinal fluid system, J. Biomech. Eng 127 (2005) 264–269. [PubMed: 15971704]

[45]. Levine DN, Intracranial pressure and ventricular expansion in hydrocephalus. Have we been asking the wrong question? J. Neurol. Sci 269 (2008) 1–11. [PubMed: 18234229]

[46]. Trippa G, Ventikos Y, Taggart DP, Coussios C-C, CFD modeling of an ultrasonic separator for the removal of lipid particles from pericardial suction blood, IEEE Trans. Biomed. Eng 58 (2011) 282–290. [PubMed: 20679023]

[47]. Landau LD, Lifshitz EM, Fluid Mechanics, Pergamon, Oxford, 1987.

[48]. Jana A, Raman A, Dhayal B, Tripp S, Reifenberger R, Microcantilever mechanics in flowing viscous fluid, Appl. Phys. Lett 114110 (2007) 1–3.

[49]. Ekinci KL, Yakhot V, Rajauria S, Colosqui C, Karabacak DM, High-frequency nanofluidics: a universal formulation of the fluid dynamics of MEMS and NEMS, Lab Chip (2010) 3013–3025. [PubMed: 20862440]

[50]. Hermanson GT, Bioconjugate Techniques, Academic Press, London, 2008.

[51]. Deshpande MD, Vaishnav RN, Submerged laminar jet impingement on a plane, J. Fluid Mech 114 (1982) 213–236.

[52]. Koga H, Mukawa J, Nakata M, Sakuta O, Higa Y, Analysis of retained ventricular shunt catheters, Neurol. Med. Chir. (Tokyo) 32 (11) (1992) 824–828. [PubMed: 1280340]

[53]. Kossovsky N, Snow RB, Clinical–pathological analysis of failed central nervous system fluid shunts, J. Biomed. Mater. Res 23 (A1) (1989) 73–86. [PubMed: 2722906]

[54]. von Recum AF, van Kooten TG, The influence of micro-topography on cellular response and implications for silicone implants, J. Biomater. Sci. Polym. Ed 7 (2) (1995) 181–198. [PubMed: 7654632]

[55]. Rahman A, Tseng Y, Wirtz D, Micromechanical coupling between cell surface receptor and RGD peptides, Biochem. Biophys. Res. Commun 296 (2002) 771–778. [PubMed: 12176050]

[56]. Maniotis AJ, Chen CS, Ingber DE, Demonstration of mechanical connections between integrins, cytoskeletal filaments, and nucleoplasm that stabilize nuclear structure, Proc. Natl. Acad. Sci 94 (1997) 849–854. [PubMed: 9023345]

[57]. Boettiger D, Huber F, Lynch L, Blystone S, Activation of αvβ3-vitronectin binding is a multistage process in which increases in bond strength are dependent on Y747 and Y759 in the cytoplasmic domain of β3, Mol. Biol. Cell 12 (5) (2001) 1227–1237. [PubMed: 11359918]

[58]. Weisel JW, Shuman H, Litvinov RI, Protein–protein unbinding induced by force: single-molecule studies, Curr. Opin. Struct. Biol 13 (2003) 227–235. [PubMed: 12727517]

[59]. Ying P, Yeh J, Kizhakkedathu JN, Vibration-based anti-biofouling of implants, in: Chiao M, Chiao JC. (Eds.), Biomaterials for MEMS, CRC Press, Boca Raton, FL, 2011, pp. 203–222 Ch. 9.

[60]. Tang L, Fibrin(ogen) mediates acute inflammatory responses to biomaterials, J. Exp. Med 178 (1993) 2147–2156. [PubMed: 8245787]

[61]. Brydon HL, Keir G, Thompson EJ, Bayston R, Hayward R, Harkness W, Protein adsorption to hydrocephalus shunt catheters: CSF protein adsorption, J. Neurosurg. Psychiatry 64 (1998) 643–647.

[62]. Lin J, Morris M, Olivero W, Boop F, Sanford RRA, Computational and experimental study of proximal flow in ventricular catheters, J. Neurosurg 99 (2003) 426–431. [PubMed: 12924722]

[63]. Galarza M, Giménez Á, Pellicer O, Valero J, Amigó JM, New designs of ventricular catheters for hydrocephalus by 3-D computational fluid dynamics, Child Nerv. Syst 31 (1) (2015) 37–48.

[64]. Busscher HJ, Norde W, Van Der Mei HC, Specific molecular recognition and nonspecific contributions to bacterial interaction forces, Appl. Environ. Microbiol 74 (9) (2008) 2559–2564. [PubMed: 18344352]

[65]. Dufrêne YF, Sticky microbes: forces in microbial cell adhesion, Trends Microbiol. 23 (6) (2015) 376–382. [PubMed: 25684261]

[66]. Brewer SH, Glomm WR, Johnson MC, Knag MK, Franzen S, Probing BSA binding to citrate-coated gold nanoparticles and surfaces, Langmuir 21 (20) (2005) 9303–9307. [PubMed: 16171365]

[67]. Vlasova IM, Saletsky a.M., Study of the denaturation of human serum albumin, J. Appl. Spectrosc 76 (4) (2009) 536–541.

[68]. Milyaeva OY, Gochev G, Loglio G, Miller R, Noskov BA, Influence of polyelectrolytes on dynamic surface properties of fibrinogen solutions, Colloids Surf. A: Physicochem. Eng. Aspects 532 (1) (2017) 108–115.

[69]. Moraleda B. Fernández-Montes, San Román J, Rodríguez-Lorenzo LM, Adsorption and conformational modification of fibronectin and fibrinogen adsorbed on hydroxyapatite. A QCM-D study, J. Biomed. Mater. Res. A 104 (10) (2016) 2585–2594. [PubMed: 27254464]

[70]. Bixler GD, Bhushan B, Biofouling: lessons from nature, Philos. Trans. R. Soc. A: Math. Phys. Eng. Sci 370 (1967) (2012) 2381–2417.

[71]. Casey AL, Mermel LA, Nightingale P, Elliott TSJ, Antimicrobial central venous catheters in adults: a systematic review and meta-analysis, Lancet Infect. Dis 8 (12) (2008) 763–776. [PubMed: 19022192]

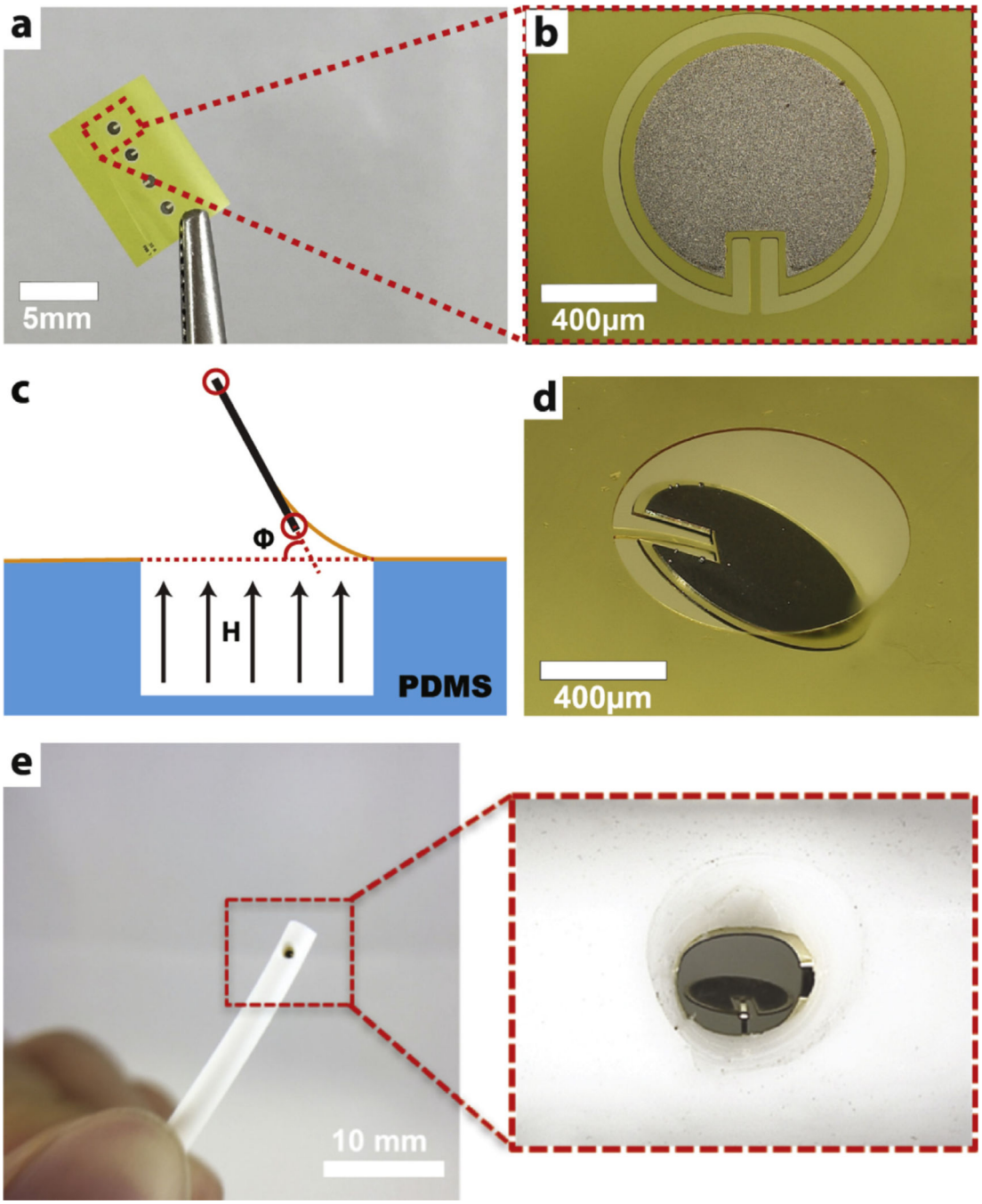

Fig. 1.

Development of self-clearing smart implantable catheter. (a) A photograph of released polyimide-based magnetic microactuator array and (b) zoomed-in view of individual device [26]. (c) Schematic of bench-top mechanical evaluation setup, which allows large out-of-plane deflection ϕ in the presence of externally applied magnetic fields. (d) A photograph of a deflected device. (e) Images of integrated thin-film magnetic microactuators into an implantable silicone-based catheter to provide self-clearing capability.

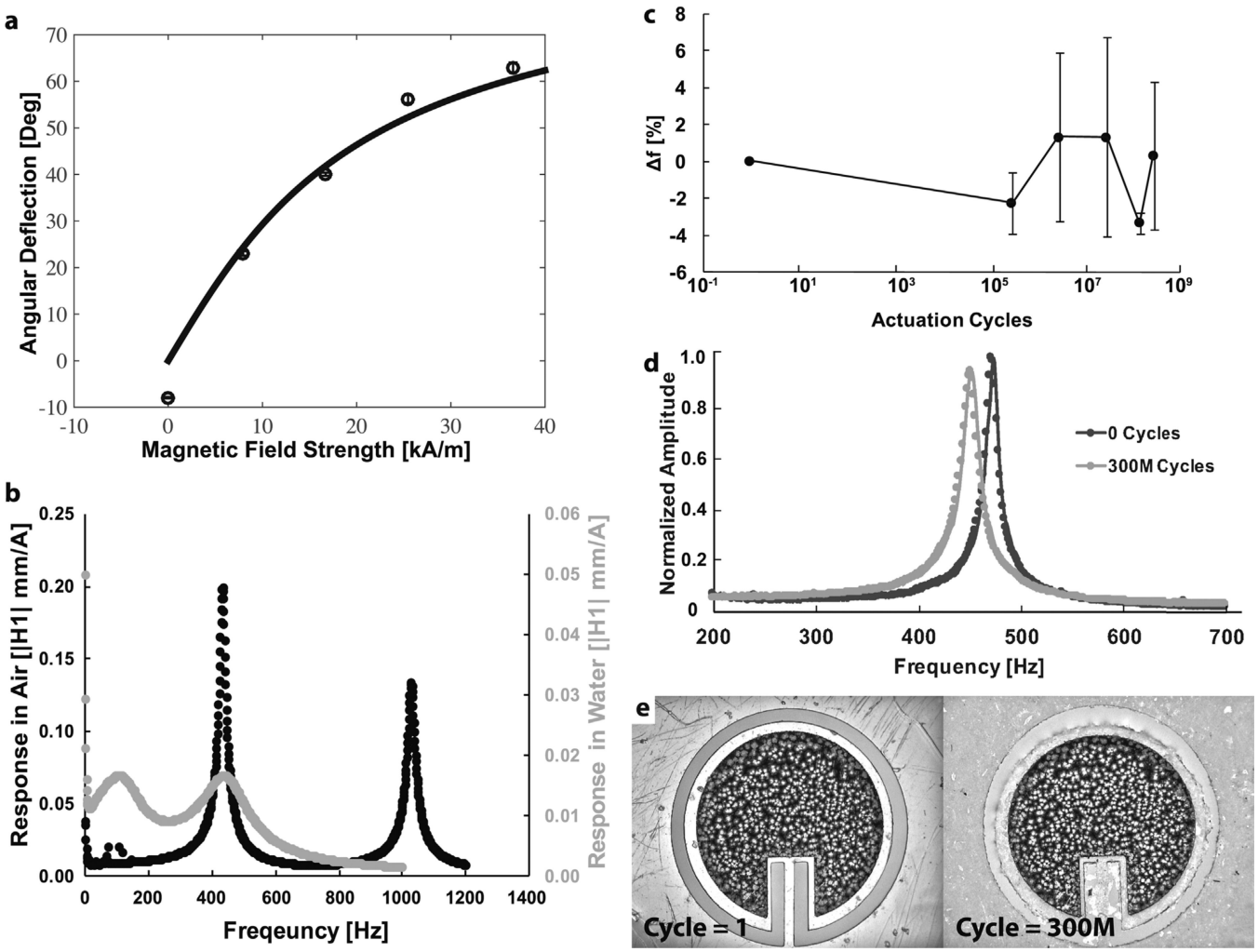

Fig. 2.

Mechanical evaluations. (a) Deflection of magnetic microactuators under static magnetic field. Solid line indicates theoretical prediction, circle represents measured values. The results (n=3) are expressed as average ± s.d. (b) H1 frequency response estimators of a representative magnetic microactuator in air and in water. Black dots and axis represent data in air, grey dots and axis represents data in deionized water. (c) Percent change in primary resonant frequency at various actuation cycles. The results (n=3) are expressed as average ± s.d. (d) Frequency responses of a representative device before and after 300 M actuation cycles. (e) Photographs of a microactuator before and after 300 M actuation cycles. Note the crystallin deposit around the perimeter of the device.

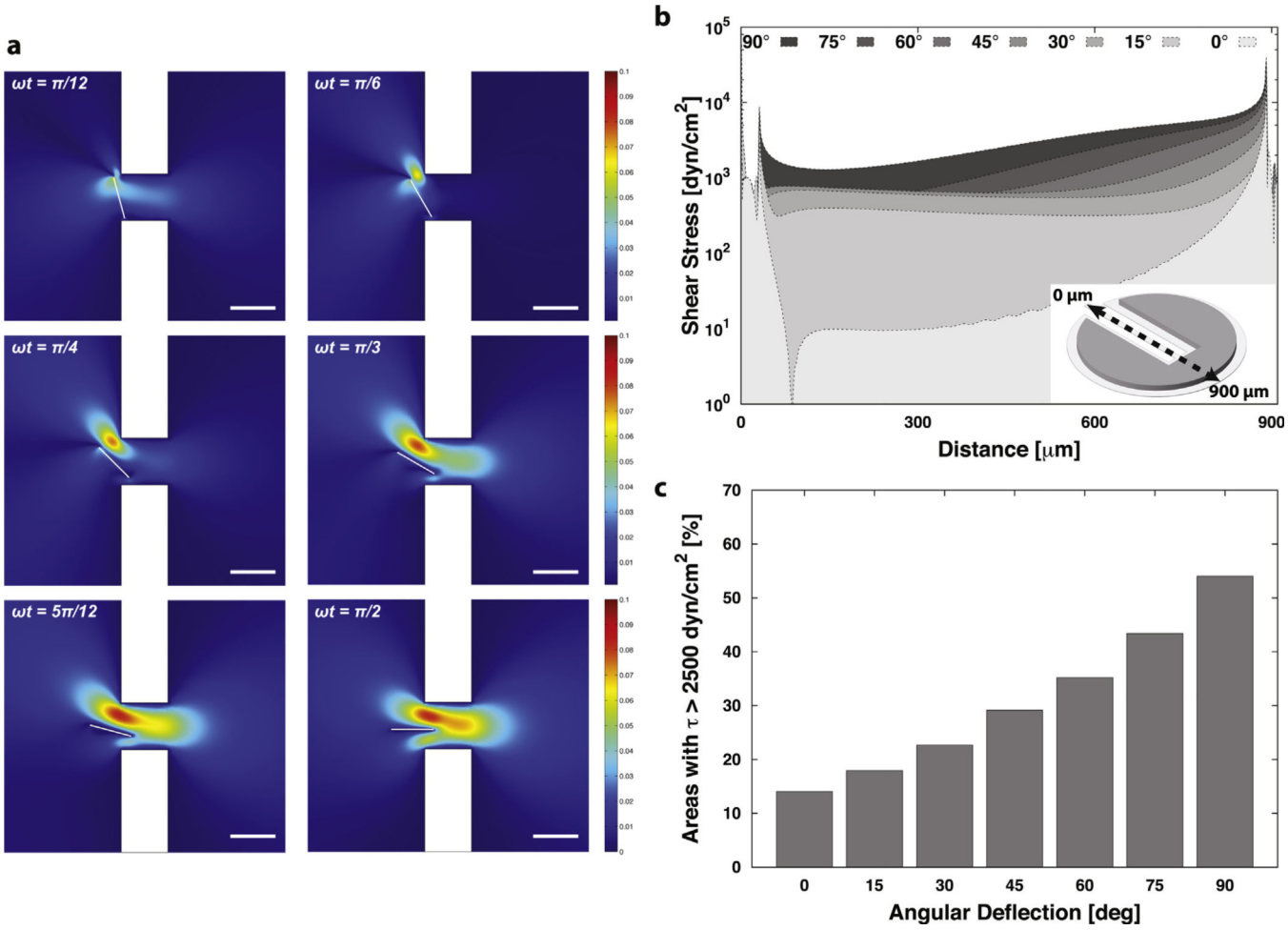

Fig. 3.

CFD results. (a) Normalized velocity field due to device actuation is plotted at different time points. The continuous flow is originating from the left boundary and the actuator is moving against the current. Scale bars = 1 mm. (b) Plot of shear stress profile along the cross section of the magnetic microactuator (inset). Note the increasing magnitude of shear stress as the angular deflection increases. (c) Percentage of area with τ >2.5 kdyn/cm^2. The percentage of the boundary with greater than 2.5 kdyn/cm^2 of shear stress. Note that at the fully deflected state (90°), more than half of the device surface experiences greater shear stress than the threshold.

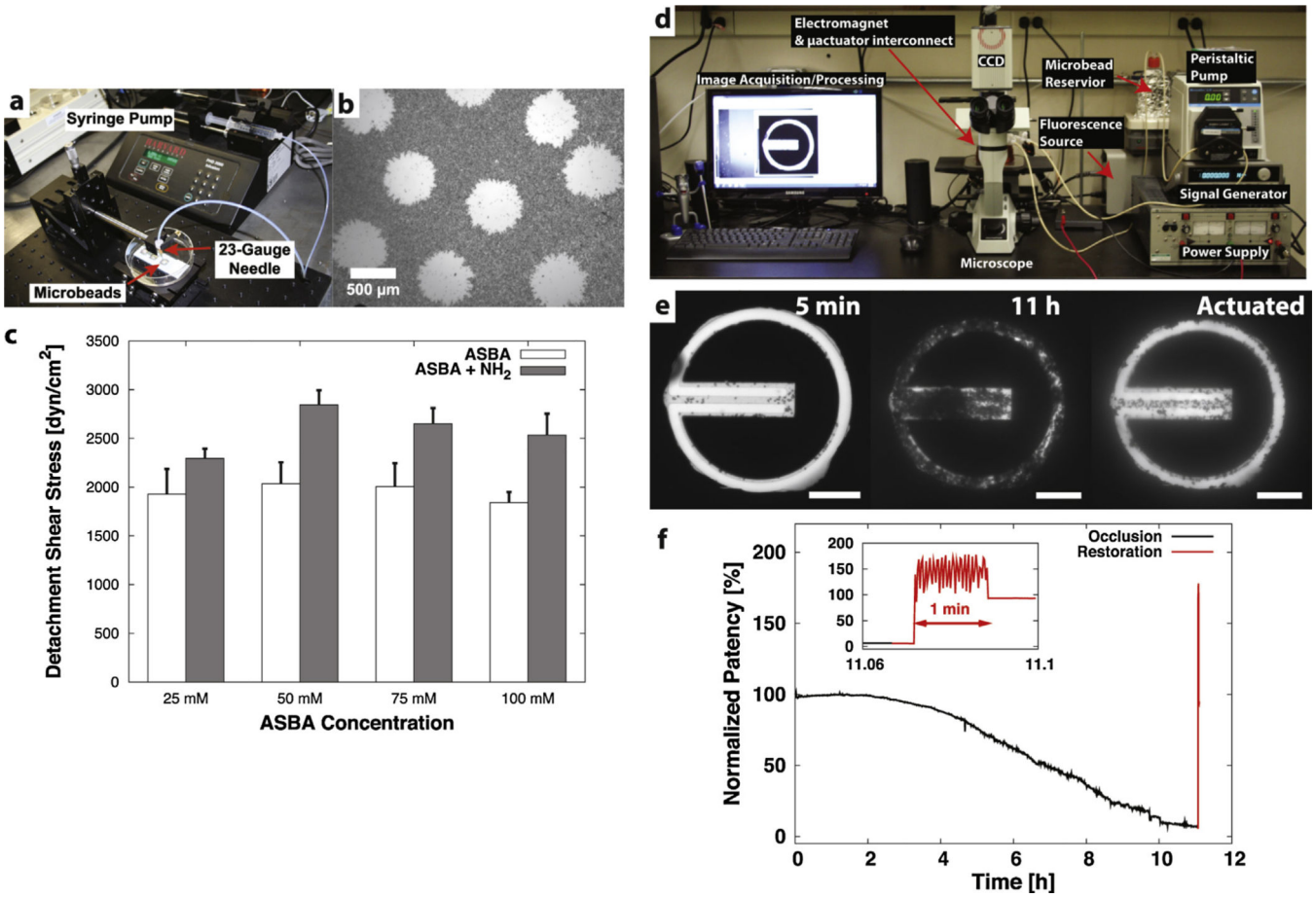

Fig. 4.

In vitro circulating biofouling model. (a) Photograph of the jet impingement experiment setup. (b) Examples of the lesions created by microfluid jets. (c) Effects of ASBA-concentration and potential cross-linking between ASBA-conjugated and NH_2-conjugated microbeads. (d) The schematic illustration of the circulating occlusion platform for evaluating the microbead clearance capabilities of magnetic microactuators. (e) Microbead removal capability of a magnetic microactuator before (at 5 min and 11 h of microbead deposition) and following actuation. Scale bars = 200 μm. (f) The amount of normalized patency as a function of time. Note the 1-minute actuation procedure (inset) restored the patency from ~10% occlusion to ~95%. The pore was normalized to when time = 0. During 1-min actuation, the magnetic microactuator deflection increased the amount of open area to be greater than 100% patency.

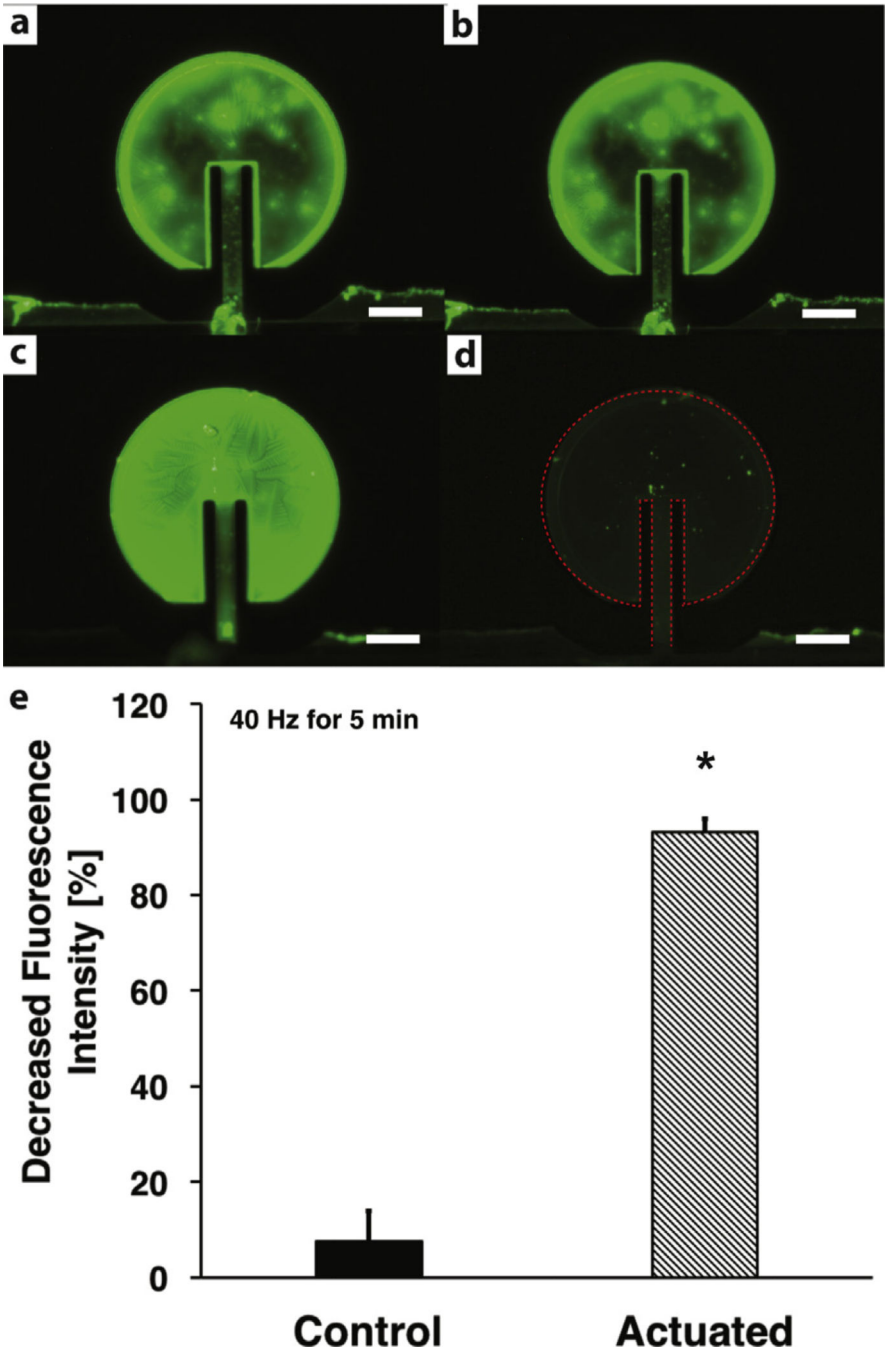

Fig. 5.

Removal of BSA-coating using microactuation. (a–d) Fluorescent images of BSA-FITC coated magnetic microactuators. Scale bar = 200 μm. The control device shows little change before (a) and after (b) treatment. The actuated device shows significant change in fluorescence intensity before (c) and after (d) application of magnetic field. Red dots outline the actuated device. (e) Plot of fluorescence reduction due to actuation (n=4). Note that the difference in fluorescence reduction between control and actuated devices is statistically

significant ($p < 0.01$). (For interpretation of the references to color in this figure legend, the reader is referred to the web version of this article.)

Table 1

Expected vs. measured resonant frequency (n=3).

	Theory	**Measured**	**Δ [%]**
Beam length [μm]	400	409.98 ± 0.75	2.49
Beam width [μm]	49	48.90 ± 0.95	−0.20
Tip mass [kg]	4.57×10^{-8}	$4.54 \times 10^{-8} \pm 3.62 \times 10^{-10}$	−0.65
J [kg m^2]	2.54×10^{-15}	$2.52 \times 10^{-15} \pm 2.02 \times 10^{-17}$	−0.78
f [Hz]	464.93	449.13 ± 7.94	−3.39